Progress In Electromagnetics Research M, Vol. 55, 25–36, 2017

Effect of Solar Illumination on ESD for Structure Used in Spacecraft

Rizwan H. Alad[1, *], Haely Shah[1], Soumyabrata Chakrabarty[2], and Dhairya Shah[1]

Abstract—This paper presents the effect of solar illumination on the differential potential generated on the surfaces of spacecraft body in space. Two geometrical cases are considered: 1) Cylindrical symmetry and 2) Tilted metallic plates forming an angle with the adjacent side. The capacitance required for estimation of the body potential is computed by Method of Moment. Nonuniform triangular meshing is used for both the geometrical structures. The differential potential generated on surfaces of a geometrical body due to photoelectric effect results in electrostatic discharge. In the case of the tilted plates, the differential potential at various tilt-angles is computed along with the capacitance computation. In the case of the cylindrical object, the estimation of potential at the day-night interface is shown. The variation in the potential for different incident angles of the solar photons and the changing (h/r) ratio is analyzed. The validity of the analysis is established with that obtained in open literature.

1. INTRODUCTION

Solar radiation from the sun has a significant effect on spacecraft charging [1]. The erratic radiation causes variation in potential among different surfaces of spacecraft which results in electrostatic discharge (ESD) [1–3]. Electrostatic discharge is a vital factor in the contribution of various anomalies caused in a spacecraft. Electrostatic discharge causes un-commanded change in system states, loss of synchronization in timing circuits, solar array damage and catastrophic destruction of sensitive circuits [4, 5]. In 1991, MARECS-A spacecraft was damaged due to electrostatic discharge [6]. Anik-E1, E2, Geo-stationary satellites had a system failure due to the electrostatic discharge [7]. Recently, in 2010, Galaxy 15 and in 2011, Echostar had a loss of mission to variations in potential on surfaces of a satellite. About 12,640 million USD have been claimed for the spacecraft anomalies and failures from 1994 to 2013 [8]. 'Chandra X-ray Observatory star tracker anomalies' in spring 2010 was caused by the outer radiation belt of energetic electron [8]. Recently, various institutes including Japan Aerospace Exploration Agency (JAXA) concluded the power system failure in ADEOS-II as a result of arcing, compelling JAXA to increase its efforts to prevent electrostatic discharge [9, 10].

For the prevention of the anomalies and for mitigating the charging of spacecrafts, various tools have been developed by numerous Space Institutes around the world, and the available charging code tools include Multi-Utility Spacecraft Charging Analysis Tool (MUSCAT), Spacecraft Plasma Interaction Software (SPIS), NASA Charging Analyzer Program (NASCAP-2K), and SEE interactive spacecraft charging handbook. NASCAP-2K computes the external potential structure and 3-D particle trajectories using Finite Element Method [11]. MUSCAT calculates the worst case charging potential by carrying out parametric runs of various environmental cases to determine that the satellite failure is due to ESD [12]. SPIS computes spacecraft charging including secondary electron, back-scattered electron, photoemission and spacecraft potential [13]. In order to diminish the effects of spacecraft charging, the ESD phenomenon of spacecraft bodies can be predicted for free space capacitance of the

Received 1 December 2016, Accepted 9 January 2017, Scheduled 24 February 2017

* Corresponding author: Rizwan Habibbhai Alad (rizwan_alad@yahoo.com).

[1] Department of Electronics & Communication, Faculty of Technology, Dharmsinh Desai University, Nadiad, Gujarat 387001, India.

[2] Antenna Systems Group, Space Applications Centre, Ahmedabad, Gujarat 380015, India.

different geometries used in spacecraft. The free-space capacitance of the tilted plates for various tilted angles using uniform rectangular meshing has been calculated in [14]. The capacitance using nonuniform triangular meshing and the temporal body potential of an artificial orbiting satellite has been computed in [15].

Electrostatic modelling of metallic bodies having different geometrical shapes is very important for the analysis of the electrostatic discharge. Capacitance used for estimation of the differential potential on the surfaces of the spacecraft is a crucial parameter for the analysis of electrostatic discharge. The solar panel generally modelled as a plate in a spacecraft is capable of rotating which makes it susceptible to electrostatic discharge as solar radiation on panel will vary. According to the Orbital Motion Limited theory, spacecraft in plasma can be modelled as cylindrical symmetry for the evaluation of electrostatic discharge at the day-night interface. During the day-night interface, as one portion of the spacecraft is in sunlit region, the impact of the photoelectron will be more than secondary electrons there, so it will develop a negligible positive potential, while in the sun-shadowed region, no effect of the photoelectrons is seen, and thus the secondary electrons cause a very high negative potential. A potential difference will be generated which results into electrostatic discharge between these two surfaces of the satellite. Hence the possibility of the electrostatic discharge is the most during the day-night interface (substorm). For the prevention of ESD, the potential on the surfaces of solar panels, for various incident angles of the solar radiation is of practical interest. The evaluation of potential for this kind of geometrical cases has not been done to the best of the authors' knowledge.

In this article, the estimation of the capacitance of the tilted plate for various tilted angles is carried out using Method of Moment (MoM). Charge distribution of tilted plate and the variation in potential on the surface for different tilted angles is shown. For a cylindrical symmetry, the computation of capacitance for different ratios of height to radius is validated by the results obtained in [16]. The differential potential generated at the day-night interface is computed. The photoelectric effect on the potential for various angles of solar illumination is also presented.

2. PROBLEM FORMULATIONS

Figure 1 shows the way in which ESD formation takes place, showing the parameters and their categorization. Spacecraft charging mainly depends on plasma parameters, altitude of orbit and day-night interface in the spacecraft body. Depending upon the type of orbit, i.e., LEO or GEO, the spacecraft charged due to secondary electrons, backscattered electron, and photoelectron varies. The net current density to the spacecraft configuration is given by

$$j_{net} = j_i + j_e + j_{ph} + j_{se} \tag{1}$$

where j_i and j_e are the current density of incident ion and electron respectively; j_{ph} is the current density of photoelectrons; j_{se} is the current density of secondary electron. When the net current density is zero, the spacecraft is considered to have zero potential with respect to plasma.

In this paper, spacecraft geometry is considered in GEO orbit. Ultraviolet radiation has an impact on the spacecraft surface as it results into photoelectron emission. As plasma density is very low in GEO, and the effect of the photoelectrons is not negligible [17].

The photoelectron current density is represented generally as,

$$j_{ph} = \alpha j_{ph0} \cos\theta \tag{2}$$

where α stands for the percentage of the solar illumination; j_{ph0} gives the material property determined by the orbit; θ is the incident angle of solar photons.

The photoelectric current depends upon the angle of the solar illumination and the material properties of the body. Photoelectrons constitute a current on the surface of the spacecraft which reduces the effect of the negative surface charging, which in turn makes photoelectrons a significant contributor in the surface charging described in Fig. 1. As the angle of the incidence of the photoelectrons changes, the current density of photoelectrons also changes resulting into a change in potential of the surface. As the cylindrical body has half of its surface in sunlit region and the other half in the sun-shadowed region, a differential voltage is created, which can be obtained by evaluating the net current density of Eq. (1).

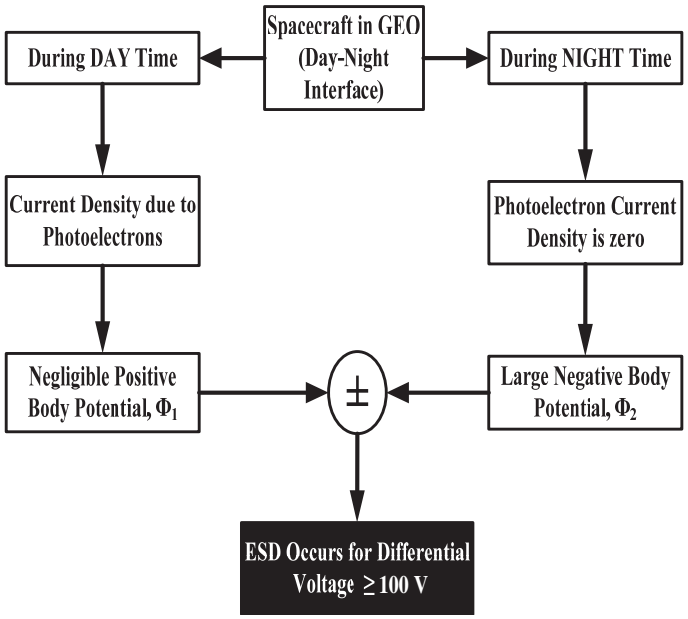

Figure 1. Effect of solar radiation in spacecraft charging.

The net current density as a function of a potential for double Maxwellian plasma in GEO is given for positive and negative saturation potential as follows [18]

$$j_{net} = \sum_{k=1}^{k=2} \left[j_{0_{ik}} \left(1 + \frac{e\,|\phi_s|}{kT_{ik}} \right) - j_{0_{ek}} e^{\left(\frac{-e|\phi_s|}{kT_{ek}} \right)} \right] + j_{ph0} \text{ when } \phi_s < 0 \tag{3}$$

$$j_{net} = \sum_{k=1}^{k=2} \left[j_{0_{ik}} \left(1 + \frac{e\,|\phi_s|}{kT_{ik}} \right) - j_{0_{ek}} e^{\left(\frac{-e|\phi_s|}{kT_{ek}} \right)} \right] + j_{ph0} e^{\left(\frac{-e\phi_s}{kT_{ph}} \right)} \left(1 + \frac{e\phi_s}{kT_{ph}} \right) \text{ when } \phi_s > 0 \tag{4}$$

For $\varphi_s = 0$, the net current will be negative which is not possible. Here, j_{0i} and j_{0e} are current densities of ion and electron respectively; j_{ph0} is current density of photoelectron; T_i and T_e are temperatures of ion and electron respectively.

As shown in Fig. 1, during the day time, the surface potential will be positive. So, roots of Eq. (3) which gives the saturation potential, are given by

$$\phi_s \approx \frac{KT_{ph}}{e} \ln \left[\frac{j_{ph0} \left(1 + \frac{e_{\phi s}}{kT_{ph}} \right)}{j_{0e}} \right] \tag{5}$$

In the given plasma environment, Eq. (5) can be simplified as follows [8]

$$\phi_s \approx \frac{kT_{ph}}{e} \tag{6}$$

By substituting the values in the above Equation (6), the approximate potential is about 2 to 5 V.

During the night time, there will not be any photoelectrons, so $j_{ph} = 0$, which results into the potential of the surface being negative ($\phi_s < 0$). Hence, saturation potential during the night time is given by [12]

$$\phi_s = -\frac{kT_e}{e} \ln \left[\sqrt{\frac{T_i}{T_e}} \frac{m_i}{m_e} \left(1 + \frac{e\phi_s}{kT_i} \right) \right] \tag{7}$$

where, m_i and m_e denote the mass of the ion and electron, respectively. Here, $\sqrt{\frac{m_i}{m_e}} = 43$ and $T_i \approx T_e$ are substituted in Eq. (7), and it gives potential around 10 to 30 kV. Due to this potential difference

created between the surfaces at the day-night interface, the electrostatic discharge occurs. Equations (5) and (7) give the saturated potential during the day and night time, respectively.

The transient potential of the geometry can be obtained by integrating the following equation by the 4th-order Runge-Kutta method.

$$\frac{d\phi}{dt} = \frac{j_{net}A}{C_{body}} \tag{8}$$

where, A is the area of geometry, and C_{body} is the capacitance of a geometry considered, which is obtained by applying MoM.

2.1. Spacecraft Modelled as Cylinder

Figure 2 shows a spacecraft modelled as a cylinder according to the Orbital Motion Limited theory [18]. The coordinate system is chosen in such a way that base of the cylinder coincides with the X-Y plane and that height of the cylinder represents the Z axis as shown in Fig. 2. The potential at any arbitrary point $r(x, y, z)$ in Fig. 2 due to charge distribution ρ at $r'(x', y', z')$ on the conductor cylindrical surface is given by [15–18],

$$V = \frac{1}{4\pi\varepsilon} \int_s \frac{\rho(r')ds}{|r - r'|} \tag{9}$$

Here 's' is the surface of the body under consideration, ρ the unknown charge distributions on the conductor surface, and V the potential on the conductor surface. For the present case, potential is determined by considering surrounding plasma potential to be zero. In order to find the capacitance of a cylinder in Fig. 2, charge distribution must be known. The unknown charge density can be obtained by solving Eq. (9) by applying MoM.

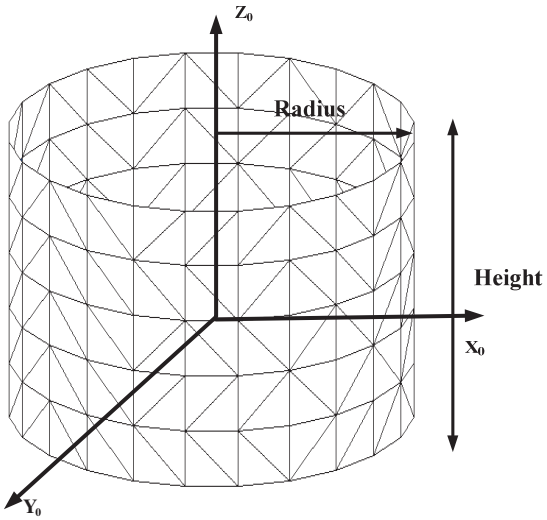

Figure 2. Spacecraft modelled as cylinder.

In order to apply the MoM, the spacecraft body is divided into a number of triangular subsections [19]. The unknown charge distribution appearing in the integral equation is expressed in terms of pulse basis function as follows:

$$\rho(r') = \sum_{n=1}^{N} \alpha_n f_n \tag{10}$$

f_n is the pulse basis functions, α_n the unknown coefficient representing the charge per unit surface area of a body under consideration and n the number of triangular sub-areas. After substituting Eq. (10)

into Eq. (9) and point matching using Dirac Delta function as testing functions, Eq. (9) is simplified as follows:

$$V = \sum_{n=1}^{N} l_{mn}\alpha_n, \quad m = 1, \ldots, n \tag{11}$$

Here, N is the number of triangular subsections in spacecraft model, suffix m the row number and n the column number. Finally, the integral equation may be expressed in matrix form as below

$$[l_{mn}]\,[\alpha_n] = [V_n] \tag{12}$$

The generalized form of coefficient appearing in the matrix Equation (12) is given as,

$$l_{mn} = \iint\limits_{Triangle} \frac{1}{\sqrt{(x_m - x_n)^2 + (y_m - y_n)^2 + (z_m - z_n)^2}} ds_n \tag{13}$$

The $r'_n(x'_n, y'_n, z'_n)$ is the coordinate of the triangular source patch and $r_m(x_m, y_m, z_m)$ the matching point on the observation triangle. The integration is evaluated in area coordinates [19], and it comprises the transformation of arbitrary shape to a canonical coordinate system. The position of the vertex node of each triangular subsection is defined by $T_1 = (x_1, y_1, z_1)$, $T_2 = (x_2, y_2, z_2)$, $T_3 = (x_3, y_3, z_3)$. Any point inside the triangle can be written by the combination of the three vertices as

$$r'_n = \gamma T_1 + \alpha T_2 + \beta T_3 \tag{14}$$

After mapping the coordinates, the expansion of area coordinates in terms of triangular vertices' components is expressed as,

$$\begin{aligned} x'_n &= (1 - \alpha - \beta)\, x_1 + \alpha x_2 + \beta x_3 \\ y'_n &= (1 - \alpha - \beta)\, y_1 + \alpha y_2 + \beta y_3 \\ z'_n &= (1 - \alpha - \beta)\, z_1 + \alpha z_2 + \beta z_3 \end{aligned} \tag{15}$$

After substituting Eq. (15) into Eq. (13), Eq. (13) can be obtained as

$$l_{mn} = \frac{|(T_2 - T_1) \times (T_3 - T_1)|}{4\pi\varepsilon} \int_0^1 \left(\int_0^{1-\alpha} \frac{1}{R} d\beta \right) d\alpha \tag{16}$$

where,

$$R = \sqrt{(x_m - x'_n)^2 + (y_m - y'_n)^2 + (z_m - z'_n)^2} = \sqrt{\left\{ \begin{array}{l} [(x_m - x_1) - (x_2 - x_1)\,\alpha - (x_3 - x_1)\,\beta]^2 \\ + [(y_m - y_1) - (y_2 - y_1)\,\alpha - (y_3 - y_1)\,\beta]^2 \\ + [(z_m - z_1) - (z_2 - z_1)\,\alpha - (z_3 - z_1)\,\beta]^2 \end{array} \right\}} \tag{17}$$

The integral in Eq. (16) is evaluated using Gauss Legendre quadrature technique.

The system of linear Equation (12) is solved by generalized minimum residual (GMRES) algorithm iterative method to find the surface charge density of each conducting surface.

Finally, the unknown charge density is expressed as,

$$[\alpha_n] = [\xi_{mn}]\,[V_n] \tag{18}$$

where ξ denotes the elements of inverse of the square moment matrix, and the charge on the plate is given by,

$$Q = \sum_{n=1}^{N} \alpha_n A_n \tag{19}$$

The free-space capacitance of a plate with respect to infinity is given by,

$$C = \frac{Q}{V} \tag{20}$$

2.2. Rectangular Metallic Plates Forming a Corner

Figure 3 shows two rectangular metallic plates of sizes $2L \times 2W$ and $2L \times 2B$ at a tilted angle θ w.r.t each other. The geometrical centre of plate-1 which is oriented along X-Y plane with perpendicular Z axis lies at the origin of the Cartesian coordinate system. Local coordinate system X-Y-Z is defined for plate-2 by rotating X-Y-Z coordinate system at an angle θ in clockwise direction. Using the transformed coordinate system, the coordinates of each and every point on plate-2 can be written in terms of global co-ordinate system. The transformed coordinates are given by,

$$\begin{aligned} x &= -x_0 \cos\theta + z_0 \sin\theta - W + B\cos\theta \\ y &= y_0 \\ z &= -x_0 \sin\theta - z_0 \cos\theta + B\sin\theta \end{aligned} \tag{21}$$

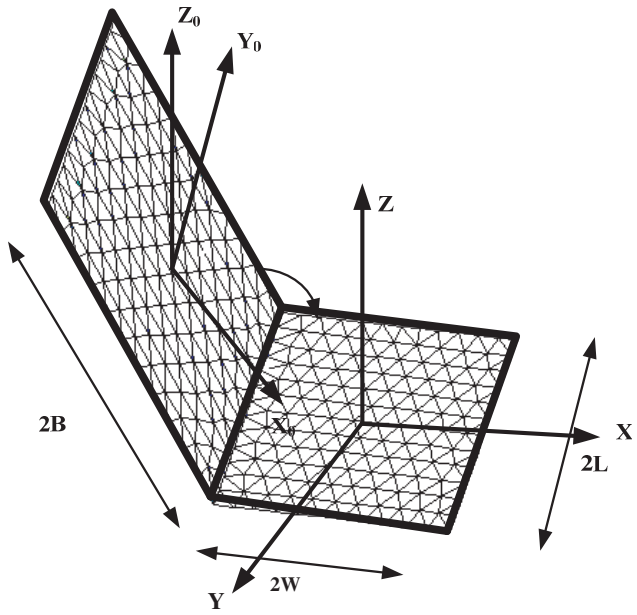

Figure 3. Co-ordinate system of tilted plates forming a corner.

These transformed coordinates are used to evaluate the capacitance using the MoM as discussed in previous section.

3. NUMERICAL RESULTS AND DISCUSSION

3.1. Cylindrical Geometry

Computation of electrostatic capacitance is done for the cylindrical structure shown in Fig. 2. A cylinder of finite dimensions (h/r) is taken. Computation is done using nonuniform triangular subsections. Cartesian axis for the structure is also shown in Fig. 2. The orbit taken into consideration is GEO where plasma density is $10^6\,\mathrm{m}^{-3}$, electron temperature 1000 eV, and the Debye length 575 m. Electrostatic capacitance for this cylinder is computed under varying ratio of height to radius using Equations (17)–(19).

Figure 4 shows the graphical representation of the variation in the free-space capacitance with changing ratio of height to radius. The capacitance drops to a very low value (here: 20 pF/m) as the ratio increases from 1 to 20. From thereon, as the ratio is increased up to 100, no great change is seen in the electrostatic capacitance. This computation is carried out by changing the height of the cylinder and keeping the radius constant ($r = 0.5$ units).

The body potential of the cylinder is also calculated for the cylinder of dimension ($r = 0.5$ units, $h = 0.5$ units). Also for the same cylinder, body potential is calculated using Eq. (8) with varying angles

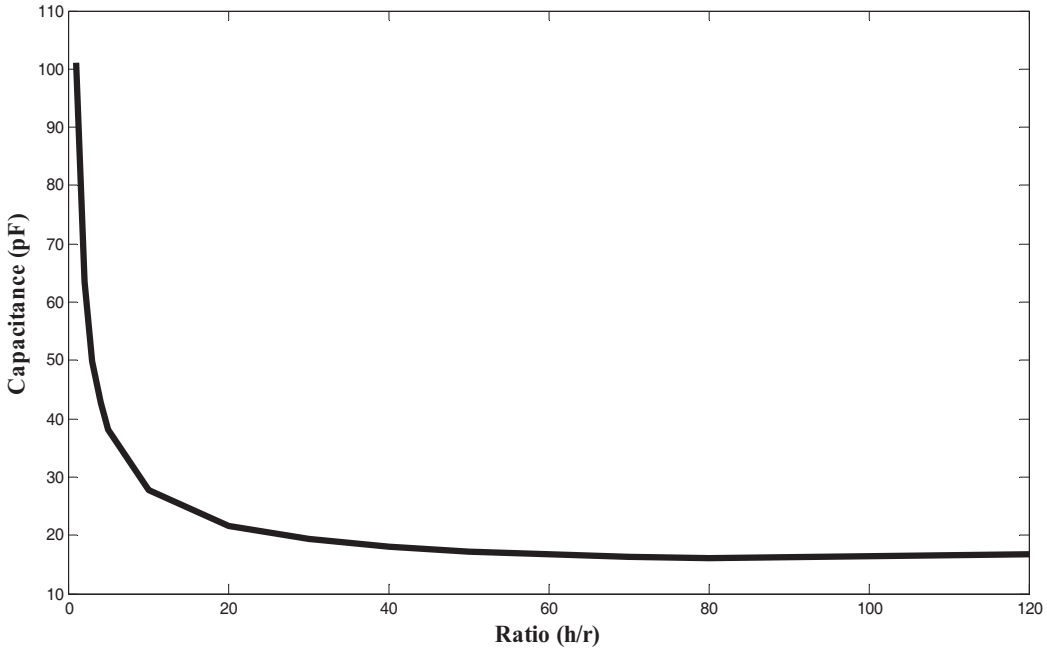

Figure 4. Variation in free space capacitance with h/r.

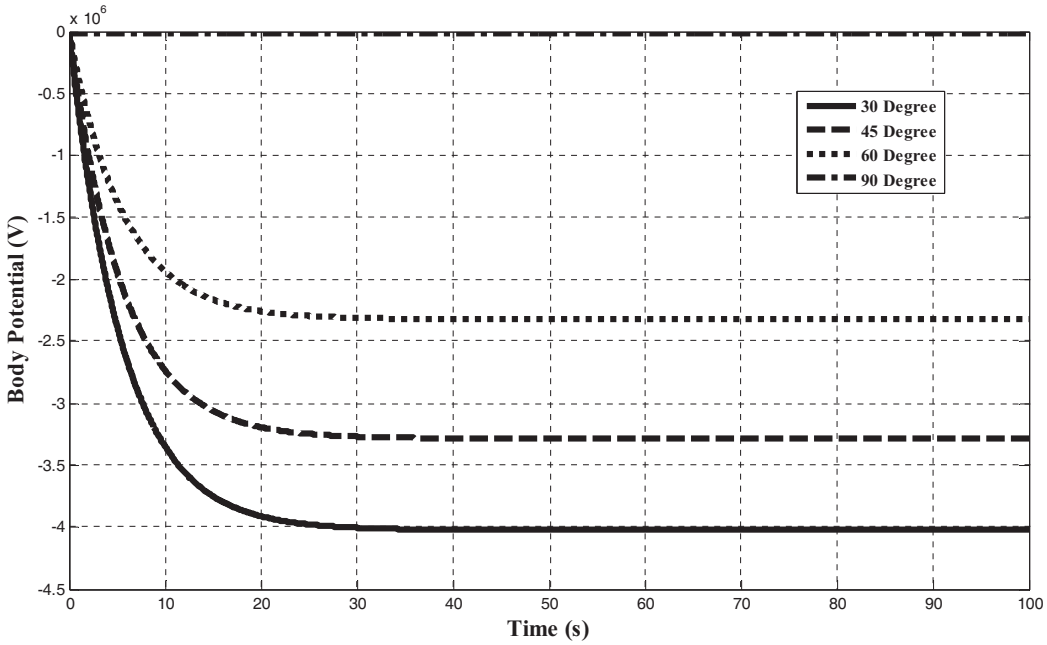

Figure 5. Body potential of the cylinder at different solar illumination angles.

the cylinder makes with solar illumination. Fig. 5 shows the plotting of body potential of angles 30, 45, 60, and 90 degrees. For 90 degrees, the body potential saturates at a value little less than -2×10^4 in about 5 seconds. For all the other values of angle made by cylindrical structure with the sun, body potential saturates in the order of 10^6 V and takes about 20 seconds.

Figure 5 also shows that as the angle decreases, the corresponding saturation voltage also decreases. This shows that when the cylinder is perpendicular to the solar illumination, chances of electrostatic charging are the highest.

Figure 6 shows the body potential of the cylinder at the interface of sunlit-sun shadowed area using Equation (7). Due to the presence of photo-electrons in the sunlit area in Eq. (6), the voltage of that side is constant at 2–5 V. As the effect of photoelectrons is prevalent only in the sunlit areas, the potential is high compared to the darker area. This creates enough threshold voltage to cause ESD.

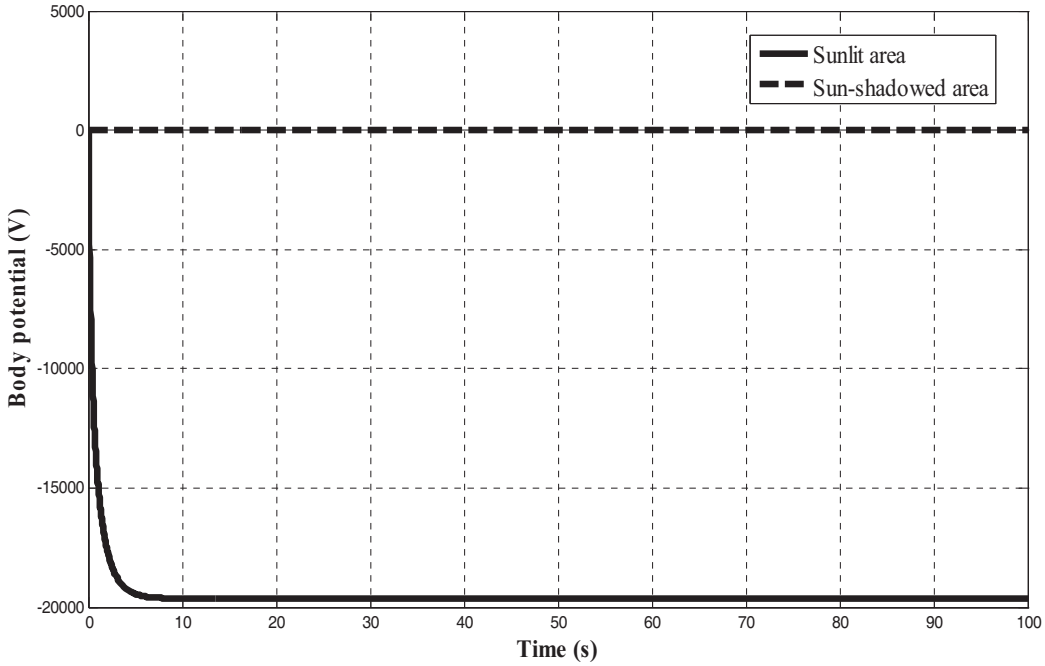

Figure 6. Body potential at sunlit and sun-shadowed surface.

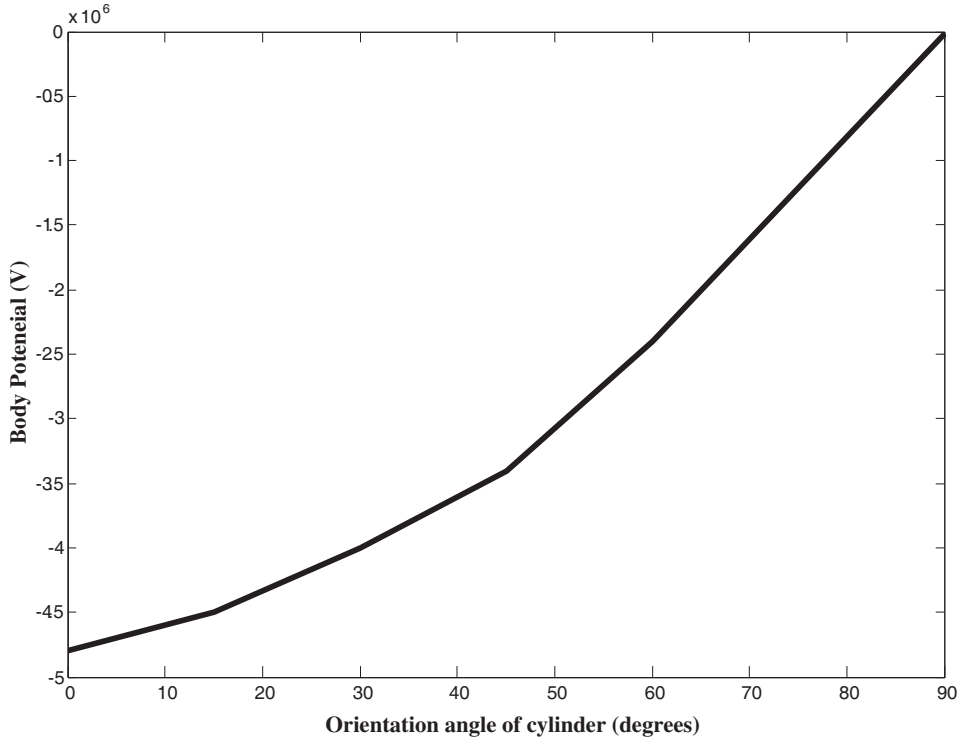

Figure 7. Variation in body potential for change in orientation angle.

Figure 7 shows the variation in saturated body potential with change in angle which the cylinder makes with the sun. At about 0, the surface is charged to its minimum. The body potential goes on increasing as the angle increases. This is because of the cosine nature of the potential. It rises to its maximum limit when the angle becomes 90 degrees. This is because a vast area of the cylindrical structure is in sunlit area.

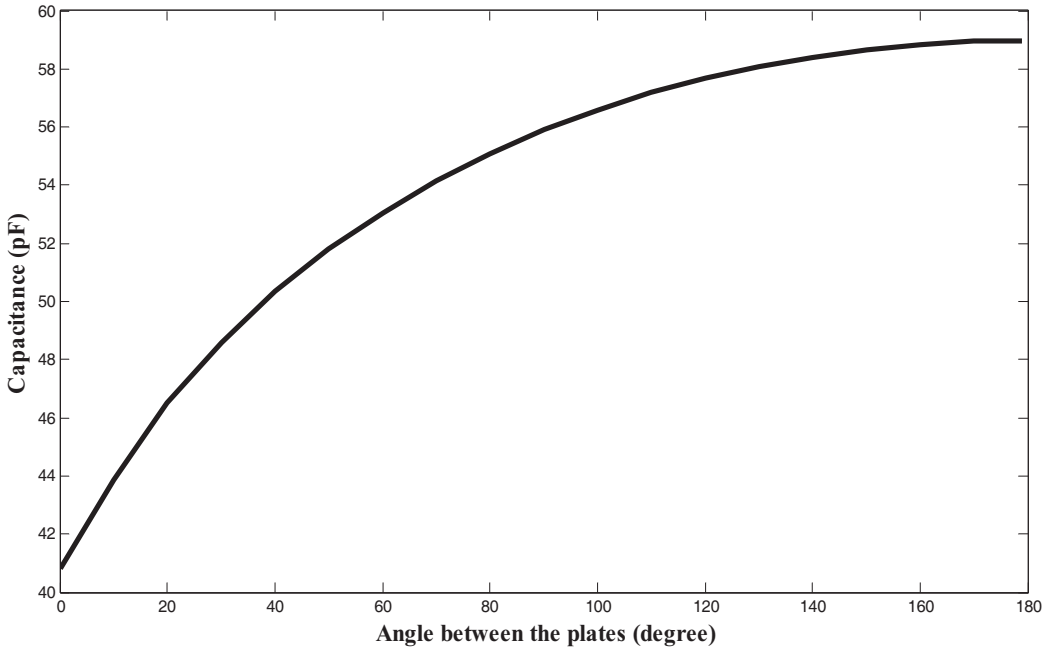

Figure 8. Variation in capacitance with angle between the plates.

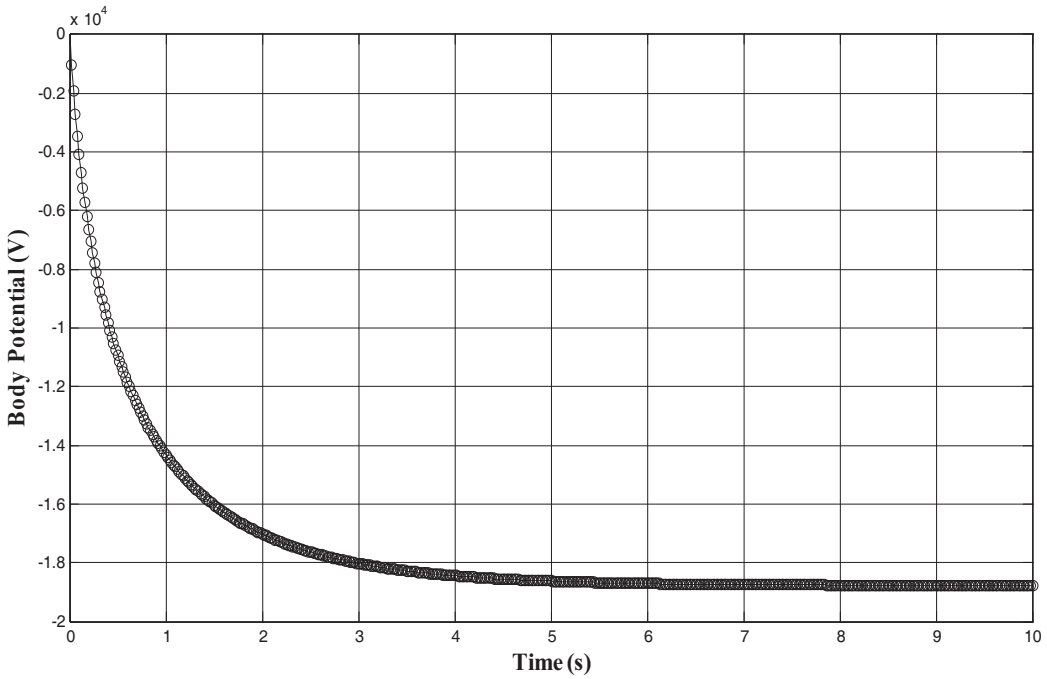

Figure 9. Body potential of tilted plate at 45.

3.2. Metallic Tilted Plates

Computation is carried out for the structure shown in Fig. 3 for two square plates each having a dimension of $L \times B = 1 \times 1\,\text{unit}^2$, and the plates are connected to each other by a side forming an angle of θ between them. The orbit taken into consideration is GEO where plasma density is $10^6\,\text{m}^{-3}$, and electron temperature is 1000 eV.

Figure 8 shows the change in the value of the capacitance of the entire structure with respect to

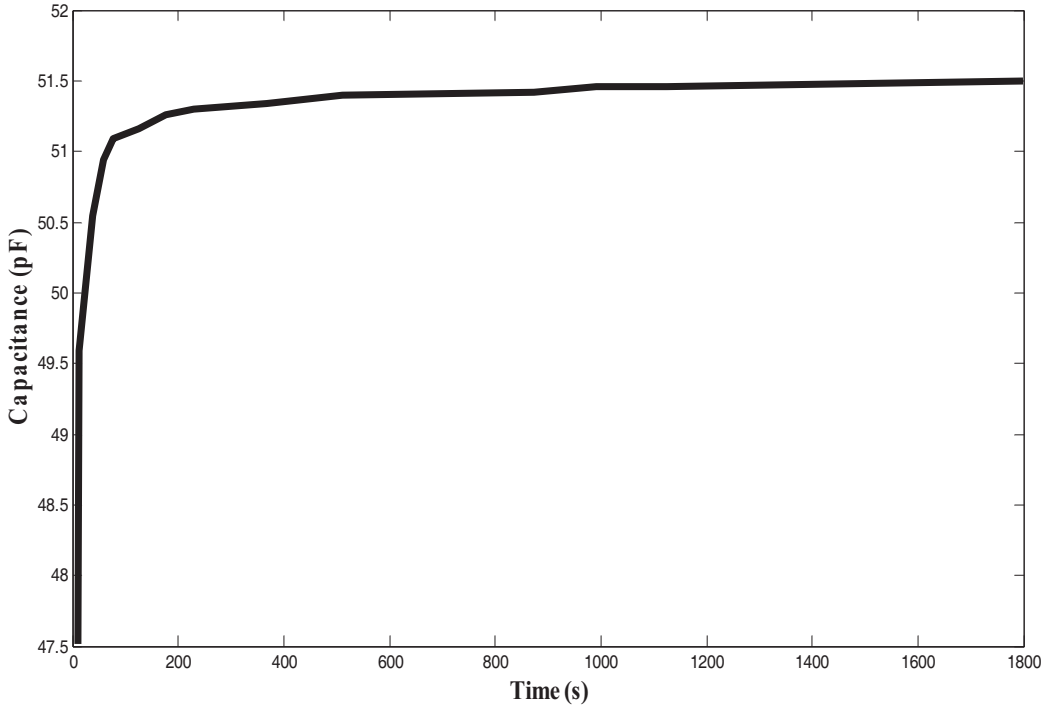

Figure 10. Capacitance of the structure at 45 with increasing number of subsections.

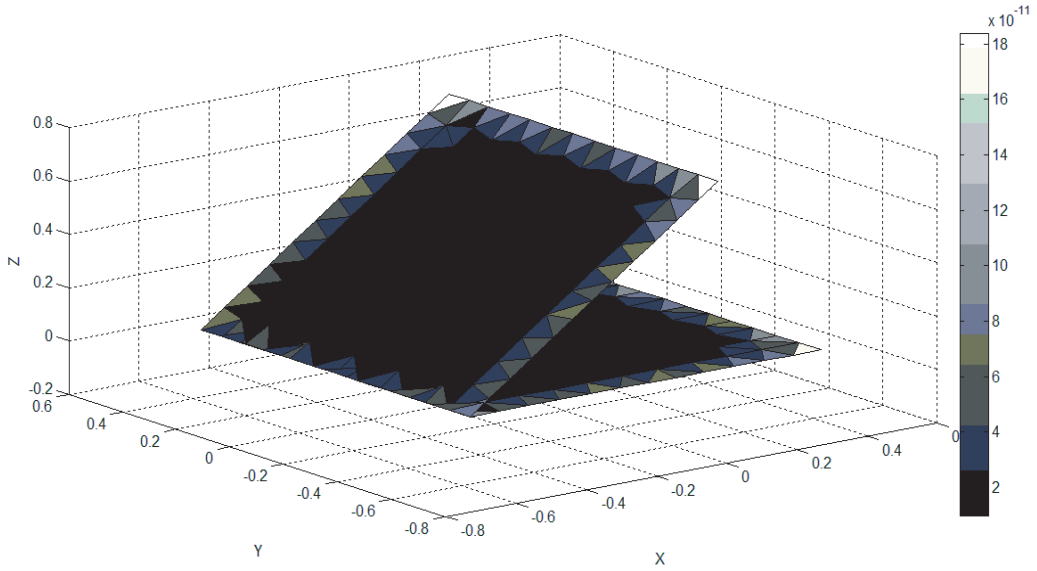

Figure 11. Charge distribution on the plates making angle of 45.

the angle between the plates. As the angle between the plates increases, capacitance increases rapidly up to a certain limit. After θ reaches a certain value, the value of capacitance is almost constant for all the subsequent angles. The convergence data of free-space capacitance are in good agreement with the result available in [14].

Figure 9 shows the body potential of plate inclined at an angle of 45 degrees. The body potential saturates at -18 kV in 4–5 seconds.

Figure 10 represents the change in capacitance of the structure with the plates forming an angle of 45 degrees with each other, with the change in subsections. As the number of subsections increases, the capacitance of the system approaches a stable and more accurate value.

Figure 11 shows the charge distribution for the same structure with $\theta = 45°$. The sides of the plates are heavily charged, and the centre of the plate is comparatively less charged.

4. CONCLUSION

The free-space capacitance and body potential are obtained for cylinder geometry and tilted plate using MoM with GMRES iterative method. This body potential is used to determine the electrostatic discharge when the geometry is under the effect of solar illumination. For the cylindrical structure, as the ratio of height to radius increases, the capacitance decreases. This result is validated with those given in open literature. The differential potential computed during the substorm shows that whenever the body is directly illuminated by solar radiation, the potential is negligibly positive. On the other hand, for a body in sun-shadowed region, the body potential is drastically reduced to several kV. For tilted plates, as the tilt-angle increases the capacitance also increases. The charge density is found to be higher at the edges of the plates than at the centre. Also, the charge is uniformly spread in the central region.

REFERENCES

1. Garrett, H. B. and A. C. Whittlesey, "Spacecraft charging, an update," *IEEE Trans. Plasma Sci.*, Vol. 28, No. 6, 2017–2028, Dec. 2000.
2. Garrett, H. B. and A. C. Whittlesey, *Guide to Mitigating Spacecraft Charging Effects (JPL Space Science and Technology Series)*, 1–28, California Inst. Technol., Pasadena, CA, USA, Jun. 2011.
3. Hastings, D. and H. Garrett, *Spacecraft-Environment Interactions*, Cambridge University Press, 1996.
4. Whipple, E. C., "Potentials of surfaces in space," *Reports on Progress in Physics*, Vol. 44, 1197–1250, 1981.
5. Fennell, J. F., J. L. Roeder, G. A. Berg, and R. K. Elsen, "HEO satellite frame and differential charging and SCATHA low-level frame charging," *IEEE Trans. Plasma Sci.*, Vol. 36, No. 5, 2271–2279, Oct. 2008.
6. Bedingfield, K. L., R. D. Leach, and M. B. Alexander, "Spacecraft system failures and anomalies attributed to the natural space environment," *NASA Reference Publication 1390*, NASA MSFC, 1996.
7. Leach, R. D. and M. B. Alexander, "Failures and anomalies attributed to spacecraft charging," *NASA Reference Publication 1354*, NASA Marshall Space Flight Center, Nov. 1994.
8. Minow, J. and L. Parker, "Spacecraft charging: Anomaly and failure mechanisms," *Spacecraft Anomalies and Failures Workshop (NASA)*, Chantilly, VA, Jul. 2014.
9. Nakamura, M., "Space plasma environment at the ADEOS-II anomaly," *Proc. 9th Spacecraft Charging Technol. Conf.*, Tsukuba, Japan, Apr. 4–8, 2005.
10. Kawakita, S., H. Kusawake, M. Takahashi, et al., "Investigation of operational anomaly of ADEOS-II satellite," *Proc. 9th Spacecraft Charging Technol. Conf.*, Tsukuba, Japan, Apr. 4–8, 2005.
11. Mandell, M. J., V. A. Davis, D. L. Cooke, A. T. Wheelock, and C. J. Roth, "Nascap-2k spacecraft charging code overview," *IEEE Trans. Plasma Sci.*, Vol. 34, No. 5, 2084–2093, Oct. 2006.

12. Muranaka, T., et al., "Development of Multi-Utility Spacecraft Charging Analysis Tool (MUSCAT)," *IEEE Trans. Plasma Sci.*, Vol. 36, No. 5, 2336–2349, Oct. 2008.
13. Roussel, J. F., F. Rogier, D. Volpert, J. Forest, G. Rousseau, and A. Hilgers, "Spacecraft Plasma Interaction Software (SPIS): Numerical solvers — Methods and architecture," *Proc. Process. 9th Spacecraft Charg. Technol. Conf.*, 462–472, Tsukuba, Japan, Apr. 2005.
14. Mehta Prarthan, D. and S. B. Chakrabarty, "Capacitance of metallic bodies forming a corner," *Journal of Applied Sciences*, 2250–2254, 2011.
15. Alad, R. H. and S. Chakrabarty, "Electrostatic analysis of an artificial orbiting satellite for absolute charging," *IEEE Trans. Plasma Sci.*, Vol. 43, No. 9, 2887–2893, Sept. 2015.
16. Chakraborty, C., D. R. Poddar, A. Chakraborty, and B. N. Das, "Electrostatic charge distribution and capacitance of isolated cylinders and truncated cones in free space," *IEEE Trans. on Electromagnetic Compatibility*, Vol. 35, No. 1, 98–102, Feb. 1993.
17. Mikaeline, T., "Spacecraft charging and hazards to electronics in space," *Physics of the Space Environment*, 1–28, York University, May 2001.
18. Hastings, D. and H. Garret, *Spacecraft Environment Interactions*, Cambridge Atmospheric and Space Sciences Series, 168, 1996.
19. Gibson, W. C., *The Method of Moments in Elecromagnetics*, 33–48, 255–269, Chapman & Hall/CRC, Taylor & Francis Group, New York, Nov. 2007.